



Research Paper

Improved steering model and integrated robust control for a curved path-tracking controller for headland turns

Yueqi Ma, Guohui Fu, Chao Ban, Tong Su, Ruijuan Chi ^{*}

College of Engineering, China Agricultural University, Beijing, 100083, China

ARTICLE INFO

Keywords:

Transplanter steering characteristics

Band-limited control

 H_∞ control

Disturbance observer

Rice transplanter

ABSTRACT

The accuracy of the rice transplanter's curved path-tracking during headland turns significantly impacts the row spacing precision of rice transplanting, especially in the initial stage of each row operation. This study aims to improve the curved path-tracking accuracy of rice transplanters. To achieve this, an improved transplanter steering model and tracking error model are developed based on the transplanter's steering characteristics, using the transplanting arm array centre as the reference point. Building upon the proposed tracking error model, an integrated robust curved path-tracking controller is proposed, combining low-frequency disturbance observer-based feedforward control, Linear Quadratic Regulator control, H-infinity control, and quadratic stability. This controller is robust to perturbation parameters and disturbances caused by uneven paddy field bottom, sideslip, path curvature, and model linearisation, and it also has a rapid convergence rate. Model comparison results indicated that the turning radii predicted by the proposed transplanter steering model closely match the actual turning radii of the rice transplanter, outperforming the conventional Ackermann steering model. Additionally, the controller using the transplanting arm array centre as the reference point exhibited higher tracking accuracy for transplanting arm array centre compared to using the rear axle centre as the reference point. Ablation experiments demonstrated the effectiveness of each component in the proposed control method, among all components, the low-frequency disturbance observer-based feedforward control had the most significant impact on accuracy improvement. Overall, the proposed curved path-tracking controller exhibited high accuracy for curved path-tracking control and effectively meets the operational requirements of the rice transplanter.

Nomenclature

(continued)

Abbreviations

Abbreviations

H_∞ Control	H-infinity Control
LMIs	Linear matrix inequalities
LQG	Linear Quadratic Gaussian
LQR	Linear Quadratic Regulator
LTR	Loop Transfer Recovery
MPC	Model Predicting Control
NSGA-II	Non-dominated Sorting Genetic Algorithm II
PID	Proportional-Integral-Derivative
PSO	Particle Swarm Optimisation
SMC	Sliding Mode Control
SSA	Sparrow Search Algorithm
Symbols	
A	Nominal state matrix of the control system

\tilde{A}	Extended state matrix
ΔA	Perturbation in the state matrix of the control system
$\Delta \tilde{A}$	Perturbation in extended state matrix
ΔA_E	Extreme points of ΔA
$\Delta \tilde{A}_E$	Extreme points of $\Delta \tilde{A}$
B	Nominal control input matrix of the control system
\tilde{B}	Extended control input matrix
ΔB	Perturbation in the control input matrix of the control system
$\Delta \tilde{B}$	Perturbation in extended control input matrix
ΔB_E	Extreme points of ΔB
$\Delta \tilde{B}_E$	Extreme points of $\Delta \tilde{B}$
C	Weighting matrix for disturbance
\tilde{C}	Extended weighting matrix for disturbance
D	Output matrix of the control system
\tilde{D}	Extended output matrix

(continued on next column)

(continued on next page)

^{*} Corresponding author.E-mail address: chiruijuan@cau.edu.cn (R. Chi).

(continued)

Abbreviations	
\hat{d}	Observed value of the disturbance
\hat{d}_l	Observed value of the low-frequency component of the disturbance
\hat{d}_{lo}	Initial value of \hat{d}_l
e_d	Lateral error, m
e_φ	Yaw angle error, rad
I	Identity matrix
K	Feedback control law gain vector
k	The curvature of the desired path, m^{-1}
L	Wheelbase, m
L_T	The distance between the rear axle centre and the transplanting arm array centre, m
L_{vir}	Virtual wheelbase, m
ΔL_i	The longitudinal distance between the inner wheel centre and front axle, m
ΔL_o	The longitudinal distance between the outer wheel centre and front axle, m
l	Observation gain coefficient of the disturbance observer
q_1	Output weight for e_φ
q_2	Output weight for e_d
R_f	Front axle centre turning radius, m
R_r	Rear axle centre turning radius, m
R_{rr}	Turning radius of the rear axle centre's desired path, m
R_T	Transplanting arm array centre turning radius, m
R_{Tr}	Turning radius of the transplanting arm array centre's desired path, m
s	Displacement of the reference point along the desired path, m
U	Control input of the control system
U_b	Feedback control input of the control system
$U_{b \max}$	The maximum value of the feedback control input
U_f	Feedforward control input of the control system
$\dot{U}_b \max$	The maximum rate of change of the feedback control input
$ U_b \max $	The absolute value of $U_b \max$
$ \dot{U}_b \max $	The absolute value of $\dot{U}_b \max$
v_r	Rear axle centre speed, $m s^{-1}$
v_T	Transplanting arm array centre speed, $m s^{-1}$
v_x	Longitudinal speed, $m s^{-1}$
$v_{x \max}$	Upper longitudinal speed bound, $m s^{-1}$
$v_{x \min}$	Lower longitudinal speed bound, $m s^{-1}$
v_{xn}	Nominal longitudinal speed, $m s^{-1}$
W	Disturbance vector of the control system
W_t	Wheel track, m
X	State vector of the control system
\tilde{X}	Extended state vector
X_{\max}	The maximum state vector
\dot{X}_{\max}	The maximum rate of change of the state vector
$ X_{\max} $	The absolute value of X_{\max}
$ \dot{X}_{\max} $	The absolute value of \dot{X}_{\max}
x	Abscissa, m
Y	Output vector of the control system
y	Ordinate, m
z	Intermediate variable of the disturbance observer
z_0	Initial value of z

Greek symbols

γ	The rotation angle of the inner steering rocker arm, rad
γ_{LQR}	Constant representing the maximum allowable H_2 norm of the disturbance-to-output transfer function.
γ_∞	Constant representing the maximum allowable H_∞ norm of the disturbance-to-output transfer function.
δ	Virtual front wheel steering angle, rad
δ_i	Inner front wheel steering angle, rad
δ_{is}	Inner front wheel slip angle, rad
δ_{iv}	Inner front wheel velocity direction angle, rad
δ_o	Outer front wheel steering angle, rad
δ_{os}	Outer front wheel slip angle, rad
δ_{ov}	Outer front wheel velocity direction angle, rad
ε	Yaw angle disturbance, $rad s^{-1}$
λ	Time constant of the low-pass filter
τ	Lateral position disturbance, $m s^{-1}$
φ	Yaw angle, rad
$\Delta\varphi_r$	The angle between the rear axle centre speed and the longitudinal speed, rad
$\Delta\varphi_T$	The angle between the transplanting arm array centre speed and the longitudinal speed, rad

(continued on next column)

(continued)

Abbreviations	
$diag(*)$	Diagonal matrix
$[*] > 0$	Matrix $[*]$ is positive definite.
$[*]^T$	Transpose of matrix $[*]$

1. Introduction

Path-tracking control technology is crucial for improving the precision of unmanned agricultural machinery operations (Bhat & Wang, 2025), such as unmanned rice transplanting. Achieving precise rice transplanting through effective path-tracking control in rice transplanters is essential for automated agriculture (Gang et al., 2022; Li et al., 2023). Currently, the straight-line path-tracking accuracy of transplanters already meets accuracy requirements (Ge et al., 2023; He et al., 2022), whereas the accuracy of curved path-tracking still requires improvement. The accuracy of the transplanter's curved path-tracking during headland turns affects the row spacing precision in the initial stage of each row operation. Therefore, research on curved path-tracking control for transplanters is of significant importance for improving the precision of unmanned rice transplanting.

In the realm of curved path-tracking for agricultural machinery, Yang et al. (2022) devised a method for determining the optimal look-ahead distance in a pure tracking algorithm, where the look-ahead area is determined by the path curvature, reducing the lateral error by more than 20 % compared to the pure tracking algorithm. Zhou et al. (2025) developed an improved pure-pursuit method for agricultural machinery, in which fuzzy control rules adjust the look-ahead distance adaptively based on path curvature and tracking errors, thereby enhancing path-tracking precision under complex curved operations. Manikandan et al. (2022) incorporated an assessment of the vehicle's proximity to the curved path into Model Predicting Control (MPC). This helps determine whether to decelerate the vehicle in advance, thus enhancing the adaptability of agricultural vehicle path-tracking control to curved paths. Zhou et al. (2023) proposed an improved MPC algorithm for articulated steering tractors that adapts time-domain parameters in real time to longitudinal speed and posture, significantly improving curved path-tracking accuracy and real-time performance. Han et al. (2019) designed a path-tracking controller for agricultural machinery based on a tyre sideslip observer, which improved the robustness of the curved path-tracking system to sideslip.

In the aforementioned research, the accuracy of curved path-tracking has been improved by optimising the controller with respect to key parameters, such as longitudinal speed, tracking error, and path curvature. Additionally, advancements in curved path-tracking systems have been achieved through disturbance observers. However, despite the significant progress made in this area, several challenges persist for unmanned rice transplanters, particularly during headland turns:

- (1) **Model accuracy:** Currently, path-tracking controllers are often designed based on the Ackermann steering model (Liu, 2001), where the front wheels steer so that their axes intersect at a point on the extension of the rear axle. However, the Ackermann steering model is an idealised steering model based on the assumption that the front wheel alignment parameters are zero. In practical rice transplanter design, its steering geometry doesn't strictly adhere to the Ackermann steering model. The angular difference in front wheel steering angles is smaller than that in the Ackermann steering, with this error increasing as the front wheel steering angle increases. As a result, controllers based on the Ackermann steering model tend to exhibit lower accuracy in the transplanter's curved path-tracking control, particularly during headland turns where the front wheel steering angles are large.

- (2) **Reference point:** Previous research has generally used the rear axle centre as the reference point for path-tracking. However, for rice transplanters, using the transplanting arm array centre may prove more effective in achieving precise operation.

Therefore, it is essential to establish a transplanter steering model and a transplanter tracking error model using the transplanting arm array centre as the reference point, based on the steering characteristics of the transplanter, to fundamentally improve the transplanter's curved path-tracking accuracy.

In addition to accurate models, advanced curved path-tracking control algorithms play a key role in improving path-tracking accuracy. Firstly, the control algorithm should ensure a rapid convergence rate for the control system. The Linear Quadratic Regulator (LQR) control, a model-based approach, determines the optimal control law by minimising the error cost function to meet this requirement. However, despite being widely used in vehicle path-tracking, it exhibits limited robustness to disturbances and perturbation parameters. Building upon the LQR control, some researchers (Lee et al., 2019) integrated the Kalman filter, effectively attenuating the impact of sensor measurement noise on the control system. However, this approach compromises robustness to non-Gaussian disturbances. To address this issue, Wu et al. (2022) applied the Loop Transfer Recovery (LTR) technique to modify the open-loop transfer function of the Linear Quadratic Gaussian (LQG) control system, thereby improving its robustness. Nevertheless, the robustness of this approach to perturbation parameters and disturbances remains fundamentally constrained by the limitations of the LQR control. When controlling a transplanter to track a curved path at the headland in the paddy field, perturbation parameters and disturbances exist due to factors such as uneven paddy field bottom, sideslip, path curvature and model linearisation. Therefore, in controller design, besides ensuring a rapid convergence rate, the system's robustness requirements for perturbation parameters and disturbances must be considered. Integrating robust control algorithms into the LQR control can offer a viable solution.

Currently, methods to improve the robustness of path-tracking controllers for agricultural machinery generally involve augmenting traditional algorithms, such as Proportional-Integral-Derivative (PID) control and pure pursuit, with fuzzy control (Dekhterman et al., 2024; Zhou et al., 2025), neural networks (Shojaei & Taghavifar, 2022), Particle Swarm Optimisation (PSO) (Gökçe et al., 2021), Sparrow Search Algorithm (SSA) (Song et al., 2025), and Non-dominated Sorting Genetic Algorithm II (NSGA-II) (Hu et al., 2024). These experience-based methods require iterative adjustments, consume significant time, lack rigorous mathematical proof, and may not easily converge to an optimal solution. Sliding Mode Control (SMC) (Ji et al., 2023; Oh and Seo, 2022), known for improving system robustness to disturbances, will induce residual oscillations in the front wheel steering angle, which are difficult to eliminate. Methods for improving the robustness of MPC-based controllers (Xu et al., 2021; Yang et al., 2019) generally achieve good results in simulation environments. However, in practical applications, they often require advanced hardware specifications because of their high computational demands. Some researchers (Han et al., 2019; Li et al., 2023) have used disturbance observers to estimate the disturbances during the path-tracking process of agricultural machinery and compensate for the control input, thereby improving the robustness of the path-tracking control system. This compensation, acting as feed-forward control, is effective for addressing low-frequency disturbances but is less effective against high-frequency disturbances. Therefore, during the controller design, a low-frequency disturbance observer-based feedforward control can be employed to compensate for specific low-frequency disturbances.

The H-infinity (H_∞) control is a robust control algorithm. It can improve system robustness to disturbances within any specified frequency band by minimising the infinity norm of the transfer function from the disturbance to the output (Zhou et al., 1996). During its design,

the robustness requirements of the system to disturbances can be converted into linear matrix inequalities (LMIs). At the same time, LQR's performance objectives and control input constraints can be formulated as LMIs. Quadratic stability, which is employed to improve system robustness to perturbation parameters, can also be addressed through LMIs. This allows for a comprehensive framework where the system can be constrained to meet multiple performance objectives simultaneously, ensuring rapid convergence of the system while maintaining its robustness to perturbation parameters and disturbances. Additionally, based on LMIs, the control law gain coefficients with high numerical reliability can be efficiently solved. The H_∞ control is being applied increasingly in autonomous road vehicles and other fields, but its development in the agricultural machinery field is relatively scarce. Rath and Subudhi (2022) proposed a robust MPC control algorithm based on the H_∞ norm, which enhances the robustness of path-tracking control for unmanned underwater vehicles against environmental disturbances while ensuring adherence to control input constraints; Legrand et al. (2022) designed a path-tracking controller for off-road vehicles based on H_∞ control, improving the robustness of the controller to parameters, such as road slope, tyre lateral stiffness, and road adhesion coefficient; Gagliardi et al. (2022) developed a path-tracking controller for autonomous vehicles in car-following scenarios using H_∞ state feedback control, improving the robustness of autonomous vehicles to disturbances, such as path curvature, perturbation in lead vehicle acceleration, and longitudinal velocity, in simulation environments. In agricultural machinery, Fukumoto et al. (2022) employed H_∞ state feedback control to the arm-length control mechanism in automatic spinach harvesters. Overall, despite lacking constraints on convergence rate, the H_∞ controller has demonstrated strong robustness in the path-tracking control of autonomous road vehicles and other control applications. However, its application in unmanned rice transplanters operating in harsh paddy field environments remains unexplored. Therefore, when designing the curved path-tracking controller for transplanters, an effective approach would be to employ the H_∞ control to improve system robustness.

In summary, to improve the curved path-tracking accuracy of rice transplanter during headland turns, a transplanter steering model and a transplanter tracking error model with the transplanting arm array centre as the reference point are first established. Building upon the tracking error model, considering the controller's convergence rate requirements, as well as the robustness requirements for perturbation parameters and disturbances, an integrated robust curved path-tracking controller is proposed. This controller integrates low-frequency disturbance observer-based feedforward control, LQR control, H_∞ control, and quadratic stability. Its control law gain coefficient is solved by the LMI toolbox in MATLAB. **It is hypothesised that this novel integrated control approach will generate more effective operational path-tracking performance during headland turns than current approaches.**

2. Materials and methods

2.1. Materials

The test platform is a modified Yanmar VP6E rice transplanter (Yanmar Agricultural Equipment Co. Ltd., Osaka, Japan), with the wheelbase $L = 1.08$ m, the wheel track $W_t = 1.18$ m, as shown in Fig. 1. To achieve more precise path-tracking for the rice transplanter, the original gasoline engine is replaced with a 48V AC induction motor. Additionally, the conventional steering mechanism is replaced with an electric power steering system actuated by a DC motor-driven gear mechanism. To achieve path-tracking, the navigation system and control system are integrated. The navigation system (CHC (R) CGI-610, Shanghai Huace Navigation Technology Ltd., Shanghai, China), which consists of navigation antennas and a navigation receiver, has a positioning accuracy of ± 0.02 m, a speed accuracy of ± 0.02 m s⁻¹, and an

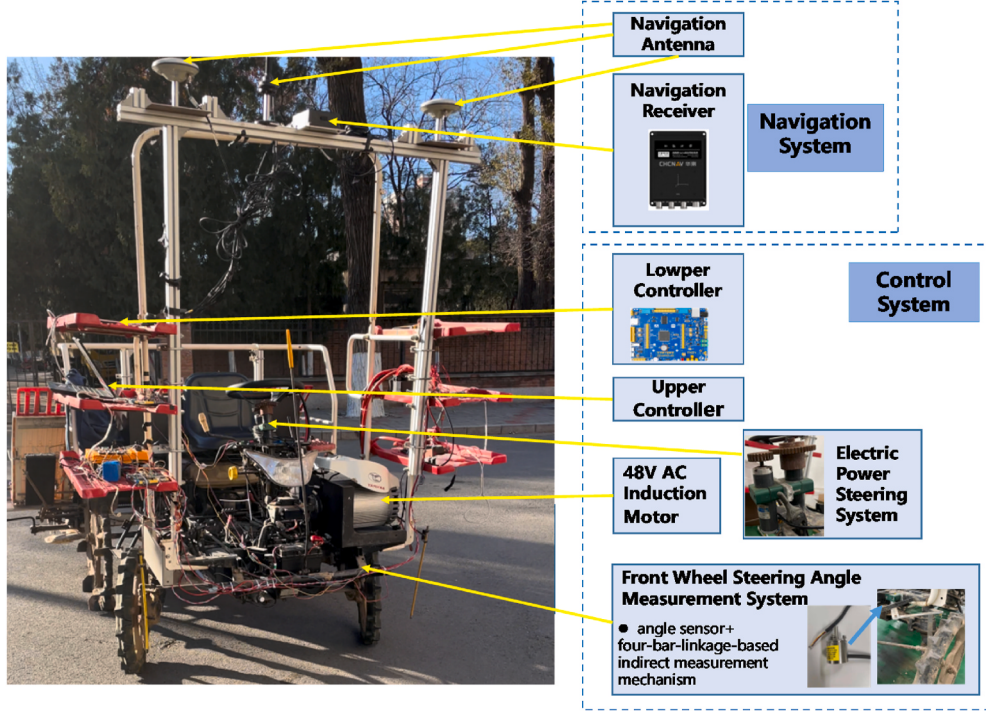


Fig. 1. Modified YANMAR VP6E transplanter, equipped with an electric steering system, drive motor, navigation system, front wheel angle measurement system, and controllers, used for path-tracking experiments.

attitude accuracy of $\pm 0.1^\circ$. In the control system, the upper controller is a personal computer (Processor: Intel (R) Core (TM) i5-9300H CPU @ 2.40 GHz, Intel Corporation, Santa Clara, CA, USA) responsible for recording experimental data. It reads the speed and passes information from the lower controller via a serial port at 10 Hz. The lower controller is an STM32F407 (STMicroelectronics, Geneva, Switzerland) microcontroller, which integrates the path-tracking control algorithm. Before each path-tracking experiment, the desired path is input into the lower controller in advance. During the path-tracking, similar to the upper controller, the lower controller receives speed and passes information from the navigation system via a serial port at 10 Hz and performs

closed-loop control of the longitudinal speed and front wheel steering angle via the CAN bus, also at 10 Hz. While controlling the front wheel steering angle, the lower controller **receives** the angle information output from the front wheel angle measurement system at 10 Hz through analogue-to-digital conversion. The front wheel angle measurement system is installed on the left front wheel, it consists of an angle sensor (RB100LA-3006-3.3, Chongqing Nuoba'en Automation Technology Co. Ltd., Chongqing, China) and a 4-bar-linkage-based indirect measurement mechanism, and the angle sensor has an accuracy of $\pm 1.08^\circ$.

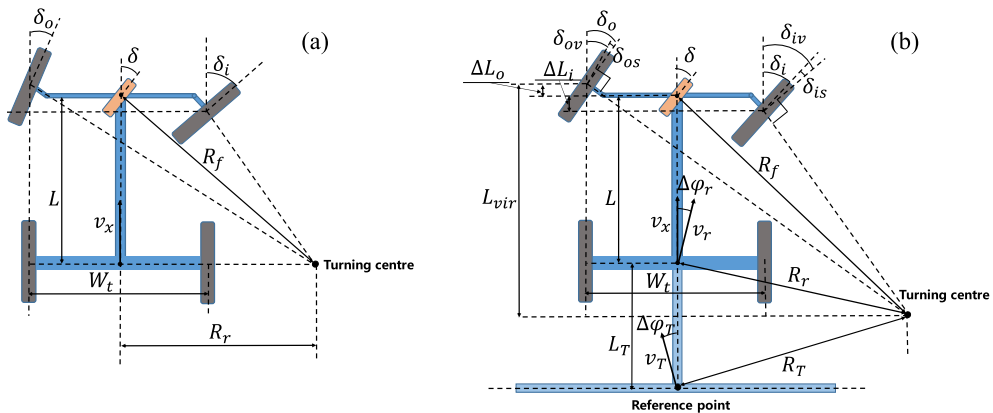


Fig. 2. Kinematic models used in this study: (a) Conventional vehicle kinematic model; (b) Transplanter steering model, where v_x is the longitudinal speed, v_r is the rear axle centre speed, v_T is the transplanting arm array centre speed, δ is the virtual front wheel steering angle, δ_o is the outer front wheel steering angle, δ_i is the inner front wheel steering angle, R_f is the front axle centre turning radius, R_r is the rear axle centre turning radius, R_T is the transplanting arm array centre turning radius, L is the wheelbase, W_t is the wheel track, L_T is the distance between the rear axle centre and the transplanting arm array centre, L_{vir} is the virtual wheelbase, ΔL_o is the longitudinal distance between the outer wheel centre and front axle, ΔL_i is the longitudinal distance between the inner wheel centre and front axle, δ_{os} is the outer front wheel slip angle, δ_{is} is the inner front wheel slip angle, δ_{ov} is the outer front wheel velocity direction angle, δ_{iv} is the inner front wheel velocity direction angle, $\Delta\varphi_T$ is the angle between the transplanting arm array centre speed and the longitudinal speed, $\Delta\varphi_r$ is the angle between the rear axle centre speed and the longitudinal speed.

2.2. System model

2.2.1. Conventional transplanter model

Assuming no sideslip and using the rear axle centre as the reference point, the conventional kinematic model of the transplanter is depicted in Fig. 2a, where δ is the virtual front wheel steering angle, δ_o is the outer front wheel steering angle, δ_i is the inner front wheel steering angle, R_f is the front axle centre turning radius, R_r is the rear axle centre turning radius. The conventional kinematic model can be derived based on geometric relationships and the Ackermann principle (Gong, et al., 2014):

$$\begin{bmatrix} \dot{x} \\ \dot{y} \\ \dot{\varphi} \end{bmatrix} = \begin{bmatrix} \cos \varphi \\ \sin \varphi \\ \tan \delta \end{bmatrix} v_x \quad (1)$$

where, x , y , φ , and v_x represent the abscissa, ordinate, yaw angle, and longitudinal speed, respectively.

Moreover, based on kinematic relationships, the conventional tracking error model can be derived (Gong et al., 2014):

$$\begin{cases} \dot{e}_\varphi = \dot{\varphi} - ks \\ \dot{e}_d = v_x \sin e_\varphi \end{cases} \quad (2)$$

where e_φ , e_d , k , s represent the yaw angle error, lateral error, curvature of the desired path, and the displacement of the reference point along the desired path, respectively. To facilitate controller design, e_φ is under the small angle assumption, and s is approximated as v_x .

Finally, by substituting $\dot{\varphi} = v_x \tan \delta / L$ in Eq. (1) into Eq. (2), the conventional simplified tracking error model, which is generally used to design path-tracking controllers, can be derived (Gong et al., 2014):

$$\begin{cases} \gamma = \angle BOG - \arcsin \frac{\overline{AG} \sin(\angle AGO + \delta_i)}{\sqrt{\overline{AG}^2 + \overline{OG}^2 - 2\overline{AG} \cdot \overline{OG} \cos(\angle AGO + \delta_i)}} - \arccos \frac{\overline{AG}^2 + \overline{OG}^2 + \overline{OB}^2 - \overline{AB}^2 - 2\overline{AG} \cdot \overline{OG} \cos(\angle AGO + \delta_i)}{2\overline{OB} \sqrt{\overline{AG}^2 + \overline{OG}^2 - 2\overline{AG} \cdot \overline{OG} \cos(\angle AGO + \delta_i)}} \\ \delta_o = \angleAGO - \arcsin \frac{\overline{OB} \sin(\angle BOG + \gamma)}{\sqrt{\overline{OB}^2 + \overline{OG}^2 - 2\overline{OB} \cdot \overline{OG} \cos(\angle BOG + \gamma)}} - \arccos \frac{\overline{AG}^2 + \overline{OG}^2 + \overline{OB}^2 - \overline{AB}^2 - 2\overline{OG} \cdot \overline{OB} \cos(\angle BOG + \gamma)}{2\overline{AG} \sqrt{\overline{OB}^2 + \overline{OG}^2 - 2\overline{OB} \cdot \overline{OG} \cos(\angle BOG + \gamma)}} \end{cases} \quad (4)$$

$$\begin{cases} \dot{e}_\varphi = \frac{v_x \tan \delta}{L} - kv_x \\ \dot{e}_d = v_x e_\varphi \end{cases} \quad (3)$$

It is worth noting that: (1) In Eqs. (1)–(3), δ is calculated based on $\delta = \arctan(L / (L \cot \delta_o - W/2))$ and $\dot{\varphi} = v_x \tan \delta / L$, both of which are established under the assumption that vehicles follow the Ackermann steering principle. However, the steering mechanism of the transplanter does not strictly adhere to the Ackermann steering principle, particularly during headland turns. (2) In Eqs. (1)–(3), the model uses the rear axle centre as the reference point. However, for the rice transplanter, it is more reasonable to establish the model using the transplanting arm array centre as the reference point to improve its operational precision. Therefore, it is essential to establish a transplanter steering model and a transplanter tracking error model using the transplanting arm array centre as the reference point for the rice transplanter based on its steering characteristics, to improve the accuracy of transplanter's curved path-tracking and its operational precision.

2.2.2. Transplanter steering model

The transplanter steering model is depicted in Fig. 2b, where R_T is

the transplanting arm array centre turning radius, δ_{iv} is the inner front wheel velocity direction angle, δ_{ov} is the outer front wheel velocity direction angle, L_{vir} is the virtual wheelbase, $\Delta\varphi_T$ is the angle between the transplanting arm array centre speed direction and the longitudinal speed direction, $\Delta\varphi_r$ is the angle between the rear axle centre speed direction and the longitudinal speed direction, L_T is the distance between the rear axle centre and the transplanting arm array centre. ΔL_o , ΔL_i are the longitudinal distance between the outer wheel centre and front axle, and the longitudinal distance between the inner wheel centre and front axle, respectively, which vary with δ_o , and each of their values corresponding to δ_o can be obtained based on a simulation performed using the Automatic Dynamic Analysis of Mechanical Systems (ADAMS) software (Hexagon MSC Software, Newport Beach, CA, USA).

It is worth noting that, as shown in Fig. 2b, when the vehicle does not adhere to Ackermann steering, tyre sideslip occurs due to uncoordinated wheel motion. Therefore, the virtual front wheel steering angle should be calculated based on the wheel velocity direction angles rather than directly from the front wheel steering angles. Furthermore, since the transplanter operates at low speeds, the centrifugal force during steering can be neglected. In this context, the wheel velocity direction angle is the sum of the front wheel steering angle and the wheel sideslip angle resulting from uncoordinated wheel motion.

When the vehicle does not adhere to Ackermann steering, the relationship between front wheel steering angles depends on the steering geometry type and its parameters. The plan view of the transplanter's steering geometry schematic shown in Fig. 3. It demonstrates that the transplanter's steering mechanism utilises a disconnected steering trapezoid configuration, with steering geometry parameters provided in Table 1, where \overline{AG} and \overline{DE} are the trapezoidal arms, \overline{OB} and \overline{OC} are the steering rocker arms. Consequently, the relationship between δ_o and δ_i can be defined in Eq. (4) (Liu, 2001), where γ is the rotation angle of the inner steering rocker arm.

Wheel sideslip angles are influenced by the lateral force on each wheel. Considering that the angular difference between the transplanter's front wheel steering angles is smaller than that in the Ackermann steering, the force equilibrium principle suggests that the turning centre of the transplanter lies behind the rear axle (Miao et al., 2017), as shown in Fig. 2b. However, given that the rear wheels have significantly greater lateral stiffness compared to the front wheels, their sideslip angles are neglected. Therefore, the turning centre of the transplanter is

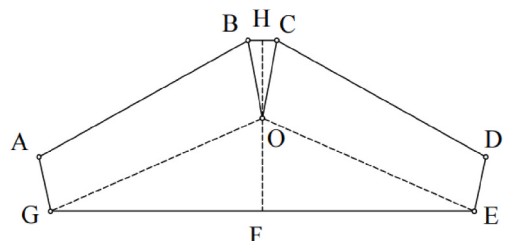


Fig. 3. Plan view of the transplanter steering geometry schematic.

Table 1
Transplanter steering geometry parameters
(corresponding to Fig. 3).

Item	value
\overline{AB}	0.600 m
\overline{OB}	0.157 m
\overline{OG}	0.570 m
\overline{AG}	0.130 m
$\angle AGO$	72.5°
$\angle BOG$	114.1°

assumed to be on the extension line of the rear axle, $L_{vir} = L$, $\Delta\varphi_r = 0^\circ$. Meanwhile, assuming that the lateral stiffnesses of the left and right front wheels are equal, then, based on the force equilibrium principle (Miao et al., 2017), the relationship between the front wheel sideslip angles and the front wheel steering angles can be derived, as shown in Eq. (5).

$$\begin{cases} R_r = \frac{L}{\tan \delta} \\ R_T = \sqrt{R_r^2 + L_T^2} \end{cases} \quad (6)$$

Finally, Eqs (4)–(6) together form the transplanter steering model.

2.2.3. Transplanter tracking error model

The schematic diagram of the transplanter tracking error model is shown in Fig. 4.

From Fig. 4 and the approach used to derive Eq. (2), by incorporating two comprehensive disturbances caused by the sideslip of the transplanter and uneven bottoms in the paddy field, i.e., yaw angle disturbance ε and lateral position disturbance τ (Li et al., 2023), the transplanter tracking error model using the transplanting arm array centre as the reference point can be derived (Eq. (7)):

$$\begin{cases} \frac{\delta_{si}}{\sin(\delta_i - \arctan(\frac{W(\tan \delta_i + \tan \delta_o)}{2W \tan \delta_i \tan \delta_o - 2(L-L_i)\tan \delta_i - 2(L+L_o)\tan \delta_o}))} = \frac{\delta_{so}}{\sin(\delta_o - \arctan(\frac{W(\tan \delta_i + \tan \delta_o)}{2W \tan \delta_i \tan \delta_o - 2(L-L_i)\tan \delta_i - 2(L+L_o)\tan \delta_o}))} \\ (L+L_o)\cot(\delta_{so} + \delta_o) - (L-L_i)\cot(\delta_{si} + \delta_i) = W \\ \delta = \arctan\left(\frac{2(L-L_i)}{2L \cot(\delta_{si} + \delta_i) + W}\right) \end{cases} \quad (5)$$

Furthermore, based on the geometric relationship, the relationship among R_r , R_T , and δ can be derived, as shown in Eq. (6).

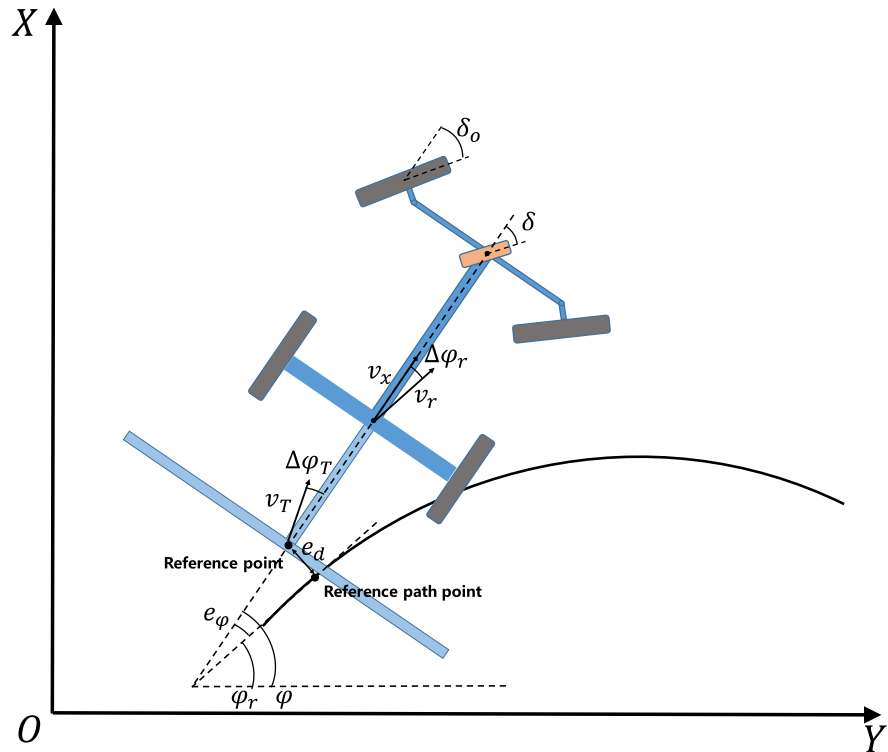


Fig. 4. Schematic diagram of the transplanter tracking error model, where e_φ is the yaw angle error, e_d is the lateral error.

$$\begin{cases} \dot{e}_\varphi = v_x \frac{\tan \delta}{L} - kv_x + \varepsilon \\ \dot{e}_d = v_T \sin(\Delta\varphi_T + e_\varphi) + \tau \end{cases} \quad (7)$$

Applying the small angle assumption for e_φ and conducting a Taylor series expansion of the second term in Eq. (7) centred at $\Delta\varphi_T$, Eq. (8) is obtained as:

$$\begin{cases} \dot{e}_\varphi = v_x \frac{\tan \delta}{L} - kv_x + \varepsilon \\ \dot{e}_d = v_T \sin\Delta\varphi_T + v_x e_\varphi + \tau \end{cases} \quad (8)$$

For controller design, Eq. (8) is transformed into the form of state-space equations:

$$\dot{X} = AX + BU + W \quad (9)$$

where, state vector $X = \begin{bmatrix} e_\varphi \\ e_d \end{bmatrix}$, state matrix $A = \begin{bmatrix} 0 & 0 \\ v_x & 0 \end{bmatrix}$, control input matrix $B = \begin{bmatrix} \frac{v_x}{L} \\ 0 \end{bmatrix}$, disturbance vector $W = \begin{bmatrix} -kv_x + \varepsilon \\ v_T \sin\Delta\varphi_T + \tau \end{bmatrix}$, control input $U = \tan \delta$, in which δ can be controlled by adjusting δ_o based on Eqs. (4) and (5). Additionally, when the tracking error model uses the rear axle centre as the reference point, then $A = \begin{bmatrix} 0 & 0 \\ v_x & 0 \end{bmatrix}$, $B = \begin{bmatrix} \frac{v_x}{L} \\ 0 \end{bmatrix}$ and $W = \begin{bmatrix} -kv_x + \varepsilon \\ \tau \end{bmatrix}$.

2.3. Problem statement

2.3.1. Perturbation parameters and disturbances

During the operation of the rice transplanter, influenced by the harsh paddy field environment, v_x does not remain constant all the time. Therefore, $v_{x \max}$ is defined as the upper longitudinal speed limit, $v_{x \min}$ as the lower longitudinal speed limit, and v_{xn} as the nominal longitudinal speed, then Eq. (9) is transformed into a parametric perturbation model, as shown in Eq. (10).

$$\dot{X} = (A + \Delta A)X + (B + \Delta B)U + W \quad (10)$$

where, the extreme points of perturbation in state matrices ΔA and ΔB as defined over the interval $[v_{x \min} - v_{xn}, v_{x \max} - v_{xn}]$ are $\Delta A_E \in \left\{ \begin{bmatrix} 0 & 0 \\ v_{x \min} - v_{xn} & 0 \end{bmatrix}, \begin{bmatrix} 0 & 0 \\ v_{x \max} - v_{xn} & 0 \end{bmatrix} \right\}$, $\Delta B_E \in \left\{ \begin{bmatrix} \frac{v_{x \min} - v_{xn}}{L} \\ 0 \end{bmatrix}, \begin{bmatrix} \frac{v_{x \max} - v_{xn}}{L} \\ 0 \end{bmatrix} \right\}$, respectively.

Besides, there is a disturbance vector $W = \begin{bmatrix} -kv_x + \varepsilon \\ v_T \sin\Delta\varphi_T + \tau \end{bmatrix}$, where $-kv_x$ is the path curvature disturbance, $v_T \sin\Delta\varphi_T$ is the linearised modelling errors, yaw angle disturbance ε and lateral position disturbance τ are caused by the sideslip of the transplanter and uneven bottoms in the harsh paddy field. Additionally, from the structure of Eq. (9), it can be seen that $-kv_x + \varepsilon$ in W is the matched disturbance, which can be directly compensated by the control input, while $v_T \sin\Delta\varphi_T + \tau$ is the unmatched disturbance, which cannot be directly compensated by the control input.

2.3.2. Control system requirements

Based on the above analysis, it is essential to design a control system that has a rapid convergence rate while maintaining strong robustness to perturbation parameters and disturbances. Furthermore, given that feedforward control is specifically effective for compensating low-frequency disturbances, it can be used to compensate for the low-

frequency component of the matched disturbance $-kv_x + \varepsilon$ in $W = \begin{bmatrix} -kv_x + \varepsilon \\ v_T \sin\Delta\varphi_T + \tau \end{bmatrix}$. The high-frequency component of $-kv_x + \varepsilon$ and the unmatched disturbance $v_T \sin\Delta\varphi_T + \tau$ can be addressed through feedback control. Additionally, the virtual front wheel steering angle and its rate of change are bounded. Therefore, the controller design should achieve the following objectives: (1) Design a feedforward control to compensate for the low-frequency component of $-kv_x + \varepsilon$. (2) Develop a feedback control that ensures the system has a rapid convergence rate and strong robustness to perturbation parameters and disturbances. (3) Ensure that the control input and its rate of change remain within specified bounds.

2.4. Design of the curved path-tracking controller

Based on the aforementioned control requirements, the control law can be designed as $U = U_f + U_b$ such that: (1) Feedforward control input U_f can compensate for the low-frequency component of the matched disturbance $-kv_x + \varepsilon$ based on a disturbance observer. (2) Feedback control input $U_b = KX$, where K is the feedback control law gain vector. (3) K ensure rapid convergence of the control system through LQR control theory. (4) K restrict the gain of uncompensated disturbances on the state variables through H_∞ control. (5) K ensure the robustness of the feedback system to parameter uncertainties through quadratic stability. (6) The bounds on the control input and its rate of change are accounted for in K . In addition, since K is subject to multiple constraints, the solution for it can be obtained through LMIs. And for ease of the controller design, Eq. (10) is rewritten as:

$$\begin{cases} \dot{X} = (A + \Delta A)X + (B + \Delta B)U + W \\ Y = DX \end{cases} \quad (11)$$

where Y is the output vector of the system, the output matrix $D = \begin{bmatrix} q_1 & 0 \\ 0 & q_2 \end{bmatrix}$, q_1 and q_2 are the weights for e_φ and e_d , respectively.

It is worth noting that, based on the form of the controlled model $\dot{X} = AX + BU + W$ and the feedback control law $U_b = KX$, the transfer function from W to X in the control system can be derived as $T_{XW}(s) = [sI - (A + BK)]^{-1}$. This is in the form of the low-pass filter and already exhibits inherent high-frequency disturbance attenuation. Therefore, in the subsequent controller design process, H_∞ control can be specifically used to optimise the robustness of the control system within the low-frequency band.

2.4.1. Low-frequency disturbance observer-based feedforward control

As previously mentioned, the low-frequency components of the matched disturbance $-kv_x + \varepsilon$ in $W = \begin{bmatrix} -kv_x + \varepsilon \\ v_T \sin\Delta\varphi_T + \tau \end{bmatrix}$ can be compensated using feedforward control. To achieve this, a disturbance observer can be used to identify the low-frequency component of $-kv_x + \varepsilon$, then the feedforward control input can be computed based on the identification result, thereby improving the system robustness. It is worth noting that traditional disturbance observers do not target specific frequency bands for filtering. Therefore, to reduce the interference of high-frequency disturbances, a low-pass filter is integrated into the disturbance observer. Finally, the disturbance observer is expressed as shown in Eq. (12):

$$\begin{cases} \dot{z} = -l(z + le_\varphi) - l \frac{v_x \tan \delta}{L} \\ \widehat{d} = z + le_\varphi \\ \widehat{d}_l = \int \frac{\widehat{d} - \widehat{d}_l}{\lambda} dt \end{cases} \quad (12)$$

where z is the intermediate variable, \widehat{d} is the observed value of $-kv_x + \varepsilon$

ε, \hat{d}_l is the observed value of the low-frequency component of $-kv_x + \varepsilon$, l is the observation gain coefficient, which needs to be positive to ensure the convergence of the observation result, λ is the time constant of the low-pass filter, which is determined by the characteristics of the feedback control system.

After the observation of the low-frequency component in $-kv_x + \varepsilon$, the feedforward control input is $U_f = \frac{-L\hat{d}_l}{v_{xn}}$.

2.4.2. LQR control

To ensure the rapid convergence rate of the system, the LQR control is employed in the design process of K . First, the cost function $J(X) = \int_0^\infty (X^T DX) dt$ is defined, and the objective of LQR control is to minimise $J(X)$. Furthermore, given that $J(X) = \int_0^\infty (X^T DX) dt$ equals $\|T_{YW}(s)\|_2^2$ (Boyd et al., 1994) in system $\begin{cases} \dot{X} = AX + CW \\ Y = DX \end{cases}$, the constraints on K , as imposed by the LQR control, are not expressed in the conventional Riccati equation form. Instead, they are formulated as LMIs, to facilitate the solution of K which ensures both rapid convergence and robustness of the system.

Lemma 1. (Boyd et al., 1994): For a given constant $\gamma > 0$ and the system state-space equation $\begin{cases} \dot{X} = AX + CW \\ Y = DX \end{cases}$, the following two conditions are equivalent:

- (1) The system is asymptotically stable, and $\|T_{YW}(s)\|_2 < \gamma$.
- (2) There exist symmetric positive matrices P and Z , such that

$$\begin{cases} AP + PA^T + CC^T < 0 \\ DPD^T - Z < 0 \\ \text{trace}(Z) < \gamma^2 \end{cases}$$

Combining Lemma 1 and the state-space equation Eq. (11) without considering parametric perturbation, $K = FP^{-1}$ that minimises $J(X)$ can be determined by solving Eq. (13) to obtain matrix F and symmetric positive matrix P . The detailed proof of this process is presented in Appendix A.

$$\begin{aligned} & \min \gamma_{LQR} \\ & \text{s.t.} \begin{cases} AP + BF + (AP + BF)^T + I < 0 \\ \begin{bmatrix} -Z & DP \\ (DP)^T & -P \end{bmatrix} < 0 \\ \text{trace}(Z) < \gamma_{LQR}^2 \end{cases} \end{aligned} \quad (13)$$

2.4.3. H_∞ control

Given the presence of the uncompensated disturbances (the high-frequency component of the matched disturbance $-kv_x + \varepsilon$ and the unmatched disturbance $v_T \sin \Delta \varphi_T + \tau$) in $W = \begin{bmatrix} -kv_x + \varepsilon \\ v_T \sin \Delta \varphi_T + \tau \end{bmatrix}$ after the feedforward control, it is essential for K to restrict the gain of these disturbances on the output. This can be achieved by H_∞ control, which minimises the infinity-norm $\|T_{YW}(s)\|_\infty$ of the transfer function $T_{YW}(s) = D[sI - (A + BK)]^{-1}$, thereby achieving robustness of the system to disturbances. Meanwhile, to optimise the robustness of the control system

within a low-frequency band, assigning a weighting matrix $C =$

$$\begin{bmatrix} \frac{1}{\lambda s + 1} & 0 \\ 0 & \frac{1}{\lambda s + 1} \end{bmatrix} \text{ to. Then the system model can be rewritten as:}$$

$$\begin{cases} \dot{X} = (A + \Delta A)X + (B + \Delta B)U + CW \\ Y = DX \end{cases} \quad (14)$$

Since the weighting matrix for disturbance vector C contains frequency domain terms, for convenience in handling, Eq. (14) without considering parametric perturbation is transformed into the form of an extended state-space equation:

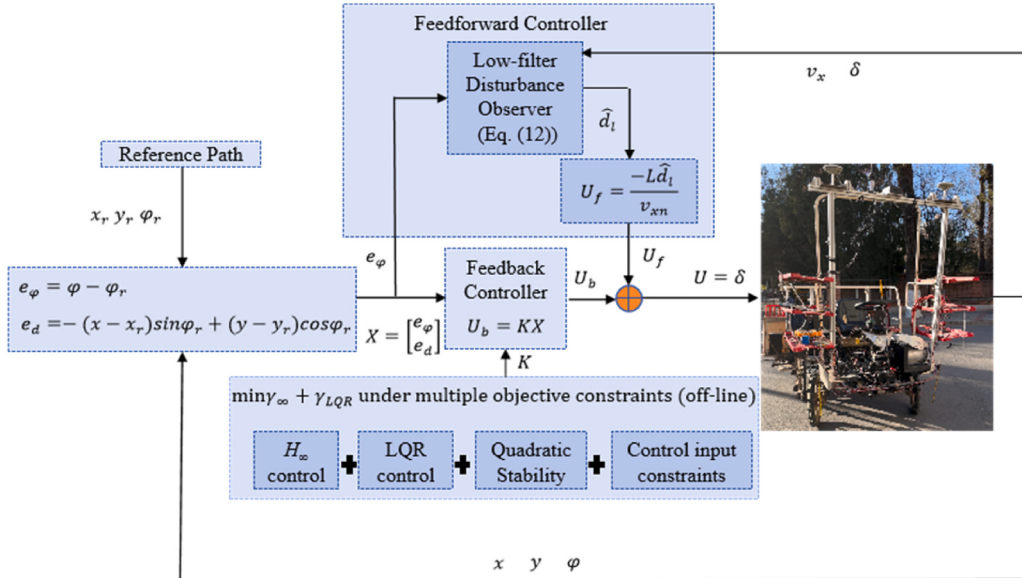


Fig. 5. Path-tracking control system block diagram, where x is the abscissa of the transplanter, y is the ordinate of the transplanter, φ is the yaw angle of the transplanter, v_x is the longitudinal speed, v_{xn} is the nominal longitudinal speed, L is the wheelbase, x_r is the abscissa of the reference path point, y_r is the ordinate of the reference path point, φ_r is the yaw angle of the reference path point, e_φ is the yaw angle error, e_d is the lateral error, X is the state vector of the control system, U is the control input of the control system, U_f is the feedforward control input of the control system, U_b is the feedback control input of the control system, δ is the virtual front wheel steering angle, K is the feedback control law gain vector, \hat{d}_l is the observed value of the low-frequency component of the disturbance.

$$\begin{cases} \dot{\tilde{X}} = \tilde{A}\tilde{X} + \tilde{B}U + \tilde{C}W \\ Y = \tilde{D}\tilde{X} \end{cases} \quad (15)$$

where extended state vector $\tilde{X} = \begin{bmatrix} X \\ W_f \end{bmatrix}$, extended output matrix $\tilde{D} = [D \ 0]$, extended state matrix $\tilde{A} = \begin{bmatrix} A & I \\ 0 & -\frac{1}{\lambda}I \end{bmatrix}$, extended control input matrix $\tilde{B} = \begin{bmatrix} B \\ 0 \end{bmatrix}$, extended weighting matrix for disturbance vector $\tilde{C} = \begin{bmatrix} 0 \\ I \\ \frac{1}{\lambda} \end{bmatrix}$.

Lemma 2. (Boyd et al., 1994): For a given constant $\gamma > 0$ and the system state-space equation $\begin{cases} \dot{X} = AX + CW \\ Y = DX \end{cases}$, the following two conditions are equivalent:

- (1) The system is asymptotically stable, and $\|Ty_w(s)\|_\infty < \gamma$.
- (2) There exists a symmetric positive matrix P , such that:

$$\begin{bmatrix} A^T P + PA & PC & D^T \\ C^T P & -\gamma I & 0 \\ D & 0 & -\gamma I \end{bmatrix} < 0$$

Combining Lemma 2 and the state-space equation Eq. (10) without considering parametric perturbation, $K = FP^{-1}$ ensuring that the disturbance has a minimum peak gain to the output Y within a low-frequency band can be determined by solving Eq. (16) to obtain matrix F and symmetric positive matrix P . The detailed proof of this process is presented in Appendix B.

$$\min \gamma_\infty$$

$$\text{s.t. } \left\{ \begin{bmatrix} (\tilde{A}P + \tilde{B}F) + (\tilde{A}P + \tilde{B}F)^T & C & (\tilde{D}P)^T \\ C^T & -\gamma_\infty I & 0 \\ \tilde{D}P & 0 & -\gamma_\infty I \end{bmatrix} < 0 \right. \quad (16)$$

2.4.4. Quadratic stability

To ensure the robustness of the controller to perturbation parameters, K must satisfy the constraints given in Eq. (13) and Eq. (16) for all possible perturbations. The problems described by Eq. (13) and Eq. (16) are convex optimisation problems, therefore, by substituting ΔA_E and ΔB_E into the combination of Eq. (13) and Eq. (16), Eq. (17) can be derived.

Table 2

Parameters used for the proposed integrated robust controller design, see Nomenclature table for description of parameters.

Parameter	Value
l	24
\hat{d}_0	0
z_0	0
λ	1
q_1	2.3
q_2	1.7
$v_x \max$	0.4
v_{xn}	0.5
$v_x \max$	0.6
$ \dot{U}_b \max $	0.6
$ U_b \max $	1.2
$ X_{\max} $	$[0.06, 0.1]^T$
$ X_{\max} $	$[0.2, 0.2]^T$

By solving Eq. (17) to obtain matrix F and symmetric positive matrix P , $K = FP^{-1}$ ensuring the system's robustness to disturbances and perturbation parameters while ensuring rapid convergence of the system can be obtained.

2.4.5. Control input constraints

Given that the virtual front wheel steering angle and its rate of change are bounded, it is essential to impose constraints on both the magnitude and the rate of change of the control input. These constraints ensure the practical implementation of the controller's output.

Let the maximum control input be denoted by U_{\max} , the maximum rate of change of the control input be denoted by \dot{U}_{\max} , the maximum state vector be denoted by X_{\max} , and the maximum rate of change of the state vector be denoted by \dot{X}_{\max} . Furthermore, U_f is ignored. Finally, $K = FP^{-1}$ must satisfy the following constraints shown in Eq. (18). The detailed proof of this process is presented in Appendix C.

$$\left\{ \begin{bmatrix} -|U_{\max}| & F \\ |X_{\max}| & P \end{bmatrix} < 0 \right. \quad (18)$$

$$\left. \begin{bmatrix} -|\dot{U}_{\max}| & F \\ |\dot{X}_{\max}| & P \end{bmatrix} < 0 \right.$$

Hence, constraints can be imposed on both the magnitude and the rate of change of the control input.

2.4.6. Overall control system and stability analysis

$$\min \gamma_\infty + \gamma_{LQR}$$

$$\text{s.t. } \left\{ \begin{bmatrix} (\tilde{A} + \Delta\tilde{A}_E)P + (\tilde{B} + \Delta\tilde{B}_E)F + ((\tilde{A} + \Delta\tilde{A}_E)P + (\tilde{B} + \Delta\tilde{B}_E)F)^T & I & (\tilde{D}P)^T \\ I & -\gamma_\infty I & 0 \\ \tilde{D}P & 0 & -\gamma_\infty I \end{bmatrix} < 0 \right. \quad (17)$$

$$\left. \begin{bmatrix} (A + \Delta A_E)P + (B + \Delta B_E)F + ((A + \Delta A_E)P + (B + \Delta B_E)F)^T + I < 0 \\ \begin{bmatrix} -Z & DP \\ (DP)^T & -P \end{bmatrix} < 0 \\ \text{trace}(Z) < \gamma_{LQR}^2 \end{bmatrix} \right.$$

where $\Delta\tilde{A}_E = \begin{bmatrix} \Delta A_E & 0 \\ 0 & 0 \end{bmatrix}$, $\Delta\tilde{B}_E = \begin{bmatrix} \Delta B_E \\ 0 \end{bmatrix}$.

By combining all the requirements for the control system outlined in Sections 2.3.1 - 2.3.5, the integrated robust control law for the curved path-tracking controller can be obtained. This control law integrates a

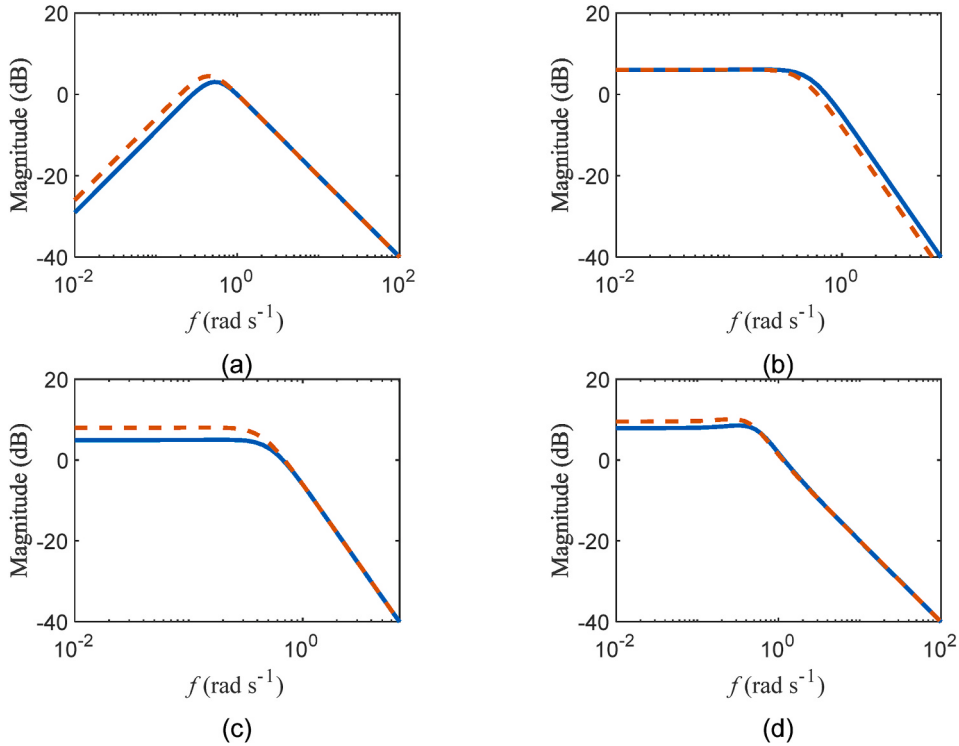


Fig. 6. The magnitude response curves of the transfer function from disturbance to state variables: (a) transfer function from $-kv_x + e$ to e_ϕ ; (b) transfer function from $-kv_x + e$ to e_d ; (c) transfer function from $v_T \sin\Delta\varphi_T + \tau$ to e_d ; (d) transfer function from $v_T \sin\Delta\varphi_T + \tau$ to e_d , where f is the frequency. The colours and styles of the curves represent different feedback controllers: red dashed line for the controller based only on LQR control; blue solid line for the controller based on Eq. (19) without quadratic stability. (For interpretation of the references to colour in this figure legend, the reader is referred to the Web version of this article.)

low-frequency disturbance observer-based feedforward control, LQR control, H_∞ control, and control input constraints. It is given as follows:

$U = U_f + U_b$, where the feedforward control input $U_f = \frac{-\hat{L}\hat{d}_l}{v_{xm}}$, in which \hat{d}_l is obtained based on Eq. (12), feedback control input $U_b = KX$, in which $K = FP^{-1}$, matrix F and symmetric positive matrix P such that

To ensure the performance and robustness of the proposed control system, stability analysis is essential. The proposed controller integrates a disturbance observer-based feedforward control to compensate for the low-frequency component of matched disturbance. As a result, the main disturbances affecting the system stability are the remaining disturbances (the high-frequency component of the matched disturbance and the unmatched disturbance). For these disturbances, a feedback

$$\begin{aligned} & \min \gamma_\infty + \gamma_{LQR} \\ & \text{s.t.} \left\{ \begin{array}{l} \left[\begin{array}{ccc} (\tilde{A} + \Delta\tilde{A}_E)P + (\tilde{B} + \Delta\tilde{B}_E)F + ((\tilde{A} + \Delta\tilde{A}_E)P + (\tilde{B} + \Delta\tilde{B}_E)F)^T & I & (\tilde{D}P)^T \\ I & -\gamma_\infty I & 0 \\ \tilde{D}P & 0 & -\gamma_\infty I \end{array} \right] < 0 \\ (A + \Delta A_E)P + (B + \Delta B_E)F + ((A + \Delta A_E)P + (B + \Delta B_E)F)^T + I < 0 \\ \begin{bmatrix} -Z & DP \\ (DP)^T & -P \end{bmatrix} < 0 \\ \text{trace}(Z) < \gamma_{LQR}^2 \\ \begin{bmatrix} -|U_{\max}| & F \\ |X_{\max}| & P \end{bmatrix} < 0 \\ \begin{bmatrix} -|\dot{U}_{\max}| & F \\ |\dot{X}_{\max}| & P \end{bmatrix} < 0 \end{array} \right. \end{aligned} \quad (19)$$

The control system block diagram is shown in Fig. 5.

controller is designed by combining H_∞ control and LQR control, and the feedback control law gain matrix K satisfies the stability requirements

Table 3

The values of feedback control law gain vector K based on different combinations of control algorithms.

Combination of control algorithms	K
LQR	[-1.28697594920258, -0.86065984703815]
LQR + H_∞	[-1.51596219915539, -1.22269598370238]
LQR + Quadratic stability	[-1.57603149419799, -0.72794414161059]
LQR + H_∞ +Quadratic stability	[-1.43849311445184, -1.13403171533097]

for both H_∞ control and LQR control, as specified in [Lemma 1](#) and [Lemma 2](#). Therefore, the proposed control system is stable.

2.4.7. Solving for the control law

During the solving process for the control law, the parameters used for controller design are shown in [Table 2](#), where \hat{d}_{l0} is the initial value of \hat{d}_l , z_0 is the initial value of z , $q_1 = 2.3$ and $q_2 = 1.7$ were determined through a comparative experiment of the control performance of different LQR controllers under various combinations of q_1 and q_2 .

The detailed solving process for K is as follows:(1) Ignore the parameter uncertainty, and solve for K based on the nominal parameter values while considering only the LQR control. Then, obtain the magnitude response curve of the transfer function from disturbances to state variables. (2) Based on the magnitude response curve of the transfer function from disturbances to state variables, determine λ . (3) Solve for K based on Eq. [\(19\)](#).

The magnitude response curves of the transfer functions from disturbances to state variables (for the control system based only on LQR control and the control system based on Eq. [\(19\)](#) without quadratic stability) are shown in [Fig. 6](#). From [Fig. 6](#), it can be observed that the cutoff frequencies of the transfer functions based only on LQR control are all at approximately 1 rad s⁻¹. Therefore, λ is set to 1. After employing the H_∞ control in the controller, the gains from $-kv_x + \varepsilon$ to e_φ , $v_T \sin\Delta\varphi_T + \tau$ to e_d , and $v_T \sin\Delta\varphi_T + \tau$ to e_d are all reduced in the low-frequency band. As for the gain from $-kv_x + \varepsilon$ to e_φ , although the reduction in the low-frequency band is not significant and there is an increase in the high-frequency band, the controller inherently suppresses high-frequency disturbances. Additionally, the feedforward control employed in this paper can compensate for the low-frequency component of $-kv_x + \varepsilon$. Consequently, the overall impact of $-kv_x + \varepsilon$ is mitigated. Therefore, the H_∞ control can improve the robustness of the controller.

Finally, the solved K based on Eq. [\(19\)](#) is shown in [Table 3](#), which also includes the values of K based on different combinations of control algorithms for further ablation experiments.

Table 4

Experimental results of model comparison between the Ackermann steering model and the proposed transplanter steering model.

Calculation basis	δ_o (°)	R_r (m)
Ackermann steering model	35	1.04
	40	0.79
	45	0.58
	50	0.41
Transplanter steering model	35	1.45
	40	1.18
	45	0.94
	50	0.67
The actual measurement results	35	1.48
	40	1.21
	45	0.95
	50	0.75

2.5. Experimental design

To validate the proposed model and proposed controller, a range of experiments are performed using the modified rice transplanter shown in [Fig. 1](#), including: (1) Comparison of different models. (2) Comparison of path-tracking controllers using different reference points. (3) Ablation study and validation of the proposed controller.

2.5.1. Comparison of different models

To verify the accuracy of the model established in this paper, a model comparison experiment is conducted. In the experiment, the outer front wheel steering angle δ_o is adjusted to 35°, 40°, 45°, and 50°, respectively. And the rear axle centre turning radius R_r corresponding to each δ_o is measured and recorded. The experiment is conducted on a concrete

Table 5

The statistical results of lateral errors of controllers using different reference points.

Controller	R_r (m)	Mean absolute value (m)	Standard deviation (m)	Mean absolute terminal value (m)	Terminal standard deviation (m)
I	2.0	0.056	0.039	0.038	0.008
II	2.0	0.091	0.049	0.142	0.009
I	1.6	0.031	0.020	0.015	0.005
II	1.6	0.074	0.083	0.156	0.010
I	1.2	0.040	0.037	0.029	0.008
II	1.2	0.048	0.064	0.133	0.011

Controller I: using rear axle centre as reference; Controller II: using transplanting arm array centre as reference.



Fig. 7. Experimental scene: (a) Actual steering radius measurement scene; (b) Path-tracking experiment scene.

Table 6

The statistical results of yaw angle errors of controllers using different reference points (Controller details given in Table 5).

Controller	R_{tr} (m)	Mean absolute value (°)	Standard deviation (°)	Mean absolute terminal value (°)	Terminal standard deviation (°)
I	2.0	2.087	1.122	1.338	1.129
II	2.0	2.881	1.368	1.768	1.676
I	1.6	2.544	0.951	1.658	1.012
II	1.6	3.901	1.680	1.849	1.681
I	1.2	1.612	0.975	1.535	1.081
II	1.2	1.895	1.428	2.099	1.640

road surface. The experimental scene is shown in Fig. 7a. The measurement process involves spraying water on the tyres and driving the transplanter in a turn, leaving a circular trajectory on the ground. Subsequently, three points are selected from the centre of the water marks, ensuring they are sufficiently spaced apart. The turning radius is then calculated using the circumcircle method. A measuring tape is used to measure the distances between the selected points. The measurement

is repeated 10 times for each δ_o , and the mean value is taken as the final result. The measurement error of the measuring tape between any two graduation marks is $\pm (0.3 + 0.2 l)$ mm, where l represents the measured distance, in metres. Then, the aforementioned δ_o are input into both the transplanter steering model proposed in this paper and the Ackermann steering model for comparison. The results are analysed to evaluate the accuracy of the proposed model.

2.5.2. Comparison of path-tracking controllers using different reference points

To assess whether using the transplanter's transplanting arm array centre as the reference point improves the unmanned transplanter's operational precision compared to using the rear axle centre, utilising the control law determination method proposed in this paper, path-tracking controllers (Controller I and Controller II) are designed based on two different tracking error models: Controller I uses the transplanting arm array centre as the reference point, while Controller II uses the rear axle centre. The comparison experiment is conducted in a paddy field located in Haidian District, Beijing, China. The wheel sinkage depth in the paddy field is approximately 0.25 m. Considering that the transplanter's paths during headland turns typically consist of quarter-circle

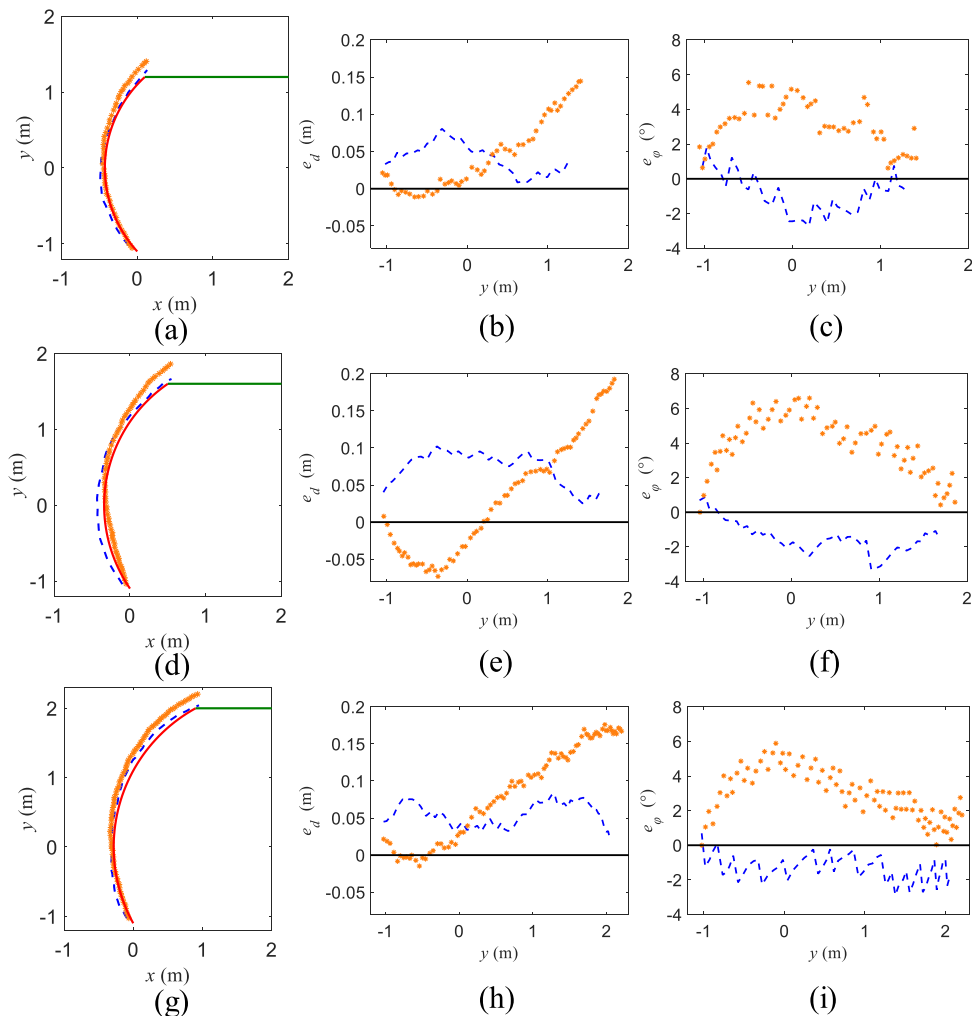


Fig. 8. Path-tracking results of controllers based on different reference points: (a)–(c) for $R_{tr} = 1.2$ m; (d)–(f) for $R_{tr} = 1.6$ m; (g)–(i) for $R_{tr} = 2.0$ m. (a), (d), and (g) show the actual paths; (b), (e), and (h) show the lateral errors; (c), (f), and (i) show the yaw angle errors. Red curves represent the desired path for the transplanting arm array centre. Green lines represent the navigation lines used as the reference for straight-line operation. The colours and styles of the other curves represent different controllers: blue line for Controller I (using rear axle centre as reference), orange * for Controller II (using transplanting arm array centre as reference). (For interpretation of the references to colour in this figure legend, the reader is referred to the Web version of this article.)

Table 7

The statistical results of lateral errors based on different controllers.

Controller	R_{rr} (m)	Mean absolute value (m)	Standard deviation (m)	Mean absolute terminal value (m)	Terminal standard deviation (m)
A	2.0	0.426	0.340	0.785	0.028
B	2.0	0.075	0.067	0.063	0.025
C	2.0	0.062	0.058	0.052	0.016
D	2.0	0.060	0.050	0.048	0.009
E	2.0	0.056	0.039	0.038	0.008
A	1.6	0.408	0.312	0.704	0.025
B	1.6	0.063	0.057	0.056	0.019
C	1.6	0.045	0.043	0.043	0.011
D	1.6	0.039	0.032	0.023	0.008
E	1.6	0.031	0.020	0.015	0.005
A	1.2	0.422	0.318	0.743	0.028
B	1.2	0.072	0.062	0.057	0.020
C	1.2	0.055	0.051	0.049	0.015
D	1.2	0.049	0.046	0.034	0.008
E	1.2	0.040	0.037	0.029	0.008

Controller A: LQR; Controller B: Disturbance observer-based feedforward control + LQR; Controller C: Disturbance observer-based feedforward control + LQR + H_∞ control; Controller D: Disturbance observer-based feedforward control + LQR + Quadratic stability; Controller E (the proposed controller in this paper): Disturbance observer-based feedforward control + LQR + H_∞ control + Quadratic stability.

Table 8

The statistical results of yaw angle errors based on different controllers (Controller details given in Table 7).

Controller	R_{rr} (m)	Mean absolute value (°)	Standard deviation (°)	Mean absolute terminal value (°)	Terminal standard deviation (°)
A	2.0	11.217	9.924	6.188	2.071
B	2.0	4.581	30.087	3.394	1.913
C	2.0	3.466	2.604	2.863	1.734
D	2.0	3.367	2.068	1.875	1.410
E	2.0	2.087	1.122	1.338	1.129
A	1.6	13.750	9.574	5.891	1.903
B	1.6	3.749	2.340	2.651	1.632
C	1.6	2.766	1.491	2.443	1.420
D	1.6	2.562	1.124	1.682	1.280
E	1.6	2.544	0.951	1.658	1.012
A	1.2	14.317	9.653	7.536	1.912
B	1.2	5.291	2.731	3.464	1.842
C	1.2	3.711	2.571	3.270	1.655
D	1.2	2.401	1.342	2.168	1.381
E	1.2	1.612	0.975	1.535	1.081

arcs and straight lines (Trendafilov & Tihanov, 2022), the quarter-circle arc in the final stage of headland turns is used as the desired path. This arc connects the navigation line used as the reference for straight-line operation. The turning radii of the rear axle centre's desired paths R_{rr} are set to 1.2 m, 1.6 m, and 2.0 m, respectively. The first point in each desired path is denoted by the coordinates (0 m, 0 m). The desired paths for the transplanting arm array centre corresponds to those of the rear axle centre. Before conducting the path-tracking experiment, each desired path is evenly discretised into 50 desired path points, and these points are input into the STM32F407 microcontroller in advance. During the experiment, the initial position of the rear axle centre and the initial yaw angle of the transplanter are (-0.04 m, 0.02 m) and 92°, respectively. The initial outer front wheel steering angles of the transplanter are 38°, 33°, and 28°, corresponding to R_{rr} of 1.2 m, 1.6 m, and 2.0 m, respectively. Besides, v_x is controlled at around 0.5 m s⁻¹ using the PID control. The experimental scenes are shown in Fig. 7b. All the tracking errors in results are calculated using the transplanting arm array centre

as the reference point. To ensure the reliability of the results, each controller is tested in 10 independent trials, and the final results are statistically obtained by taking the mean of the outcomes of these 10 trials.

2.5.3. Ablation study and validation of the proposed controller

To validate the effectiveness of the proposed controller, an ablation study is conducted by comparing it with controller variants with reduced components. The following controllers are evaluated:

Controller A: LQR.

Controller B: Disturbance observer-based feedforward control + LQR.

Controller C: Disturbance observer-based feedforward control + LQR + H_∞ control.

Controller D: Disturbance observer-based feedforward control + LQR + Quadratic stability.

Controller E (the proposed controller in this paper): Disturbance observer-based feedforward control + LQR + H_∞ control + Quadratic stability.

In all cases, the reference point for the path-tracking control is the transplanting arm array centre. The environmental conditions, sensor accuracy, initial pose, desired longitudinal speed and desired paths are consistent with those described in Section 2.5.2. The results are obtained by conducting 10 independent trials and taking the mean, in the same manner as in Section 2.5.2.

3. Results and discussion

3.1. Comparison of different models

The model comparison results are shown in Table 4. For the same δ_0 , the turning radius output by the transplanter steering model established in this paper was closer to the actual turning radius of the rice transplanter than the Ackermann steering model. Specifically, the maximum absolute error of the transplanter steering model at all tested R_r was 0.08 m, 76.5 % less than the minimum absolute error of the Ackermann steering model.

The results of the model comparison experiment demonstrated that the model established in this paper describes the motion characteristics of the rice transplanter with higher accuracy than the Ackermann steering model. Therefore, it is more appropriate for application in the design of curved path-tracking controllers for rice transplanters.

3.2. Comparison of path-tracking controllers using different reference points

The statistical results of lateral errors and yaw angle errors of controllers based on different reference points are presented in Tables 5 and 6, respectively, where the terminal value represents the results in the final 0.5 s of the tracking. The actual path curves and error variation curves presented in Fig. 8 are representative of one of the trials conducted. The experimental results indicated that for different radii of the desired paths, controlling the curved path-tracking of the rice transplanter using the transplanting arm array centre as the reference point exhibited higher path-tracking accuracy than using the rear axle centre as the reference point. For example, when $R_{rr} = 1.2$ m, the mean absolute lateral error of the transplanting arm array centre was 0.040 m, and 0.029 m in the final 0.5 s of tracking, indicating reductions of 16.7 % and 78.2 %, respectively, compared to using the rear axle centre. Additionally, the mean absolute yaw angle error of the transplanting arm array centre was 1.162°, and 1.535° in the final 0.5 s of tracking, indicating reductions of 38.7 % and 26.9 %, respectively, compared to using the rear axle centre. These results demonstrated the effectiveness of using the transplanting arm array centre as the reference point in improving path-tracking accuracy of the transplanting arm array centre. Therefore, controlling the curved path-tracking using the transplanting arm array

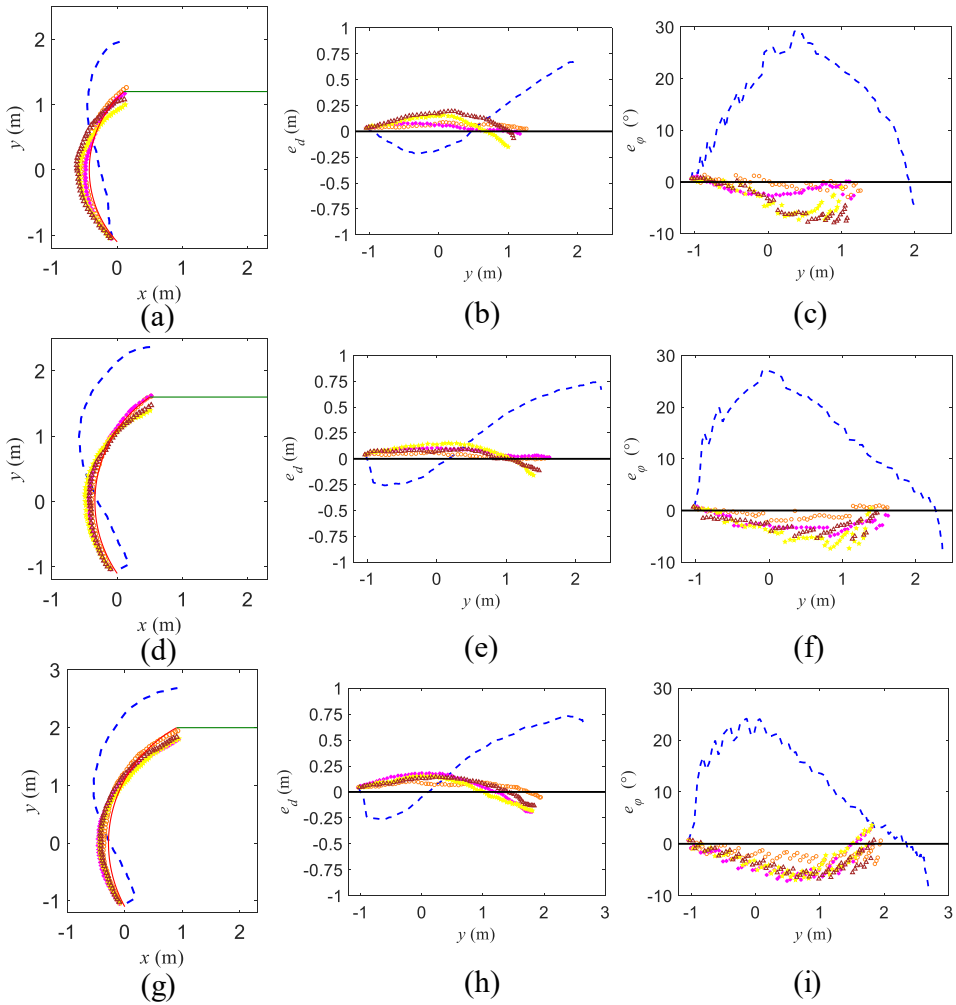


Fig. 9. Path-tracking results of controllers based on different combinations of control algorithms: (a)–(c) for $R_{rr} = 1.2$ m; (d)–(f) for $R_{rr} = 1.6$ m; (g)–(i) for $R_{rr} = 2.0$ m. (a), (d), and (g) show the actual paths; (b), (e), and (h) show the lateral errors; (c), (f), and (i) show the yaw angle errors. Red curves represent the desired path for the transplanting arm array centre. Green lines represent the navigation lines used for straight-line operation. The colours and styles of the other curves represent different controllers: blue line for Controller A (LQR), brown \triangle for Controller B (Disturbance observer-based feedforward control + LQR); yellow \star for Controller C (Disturbance observer-based feedforward control + LQR + H_∞); purple $*$ for Controller D (Disturbance observer-based feedforward control + LQR + Quadratic stability); orange \circ for Controller E (Disturbance observer-based feedforward control + LQR + H_∞ + Quadratic stability). (For interpretation of the references to colour in this figure legend, the reader is referred to the Web version of this article.)

centre as the reference point can improve the precision of the transplanting operation.

3.3. Ablation study and validation of the proposed controller

The statistical results of lateral errors and yaw angle errors based on different controllers are presented in Tables 7 and 8, respectively, where the terminal value represents the results in the final 0.5 s of the tracking. The actual path curves and error variation curves presented in Fig. 9 are representative of one of the trials conducted. The experimental results indicated that the path-tracking error was considerably larger when using LQR control alone. After incorporating low-frequency disturbance observer-based feed-forward compensation, both the lateral error and the yaw angle error were significantly reduced. Subsequently, integrating the H_∞ control into the controller further reduced tracking errors. Finally, the integration of the quadratic stability, building on previous improvements, resulted in the lowest errors. For example, when $R_{rr} = 1.2$ m, the mean absolute lateral error and the mean absolute yaw angle error with LQR control were 0.422 m and 14.31° ,

respectively. The integration of the low-pass disturbance observer-based feed-forward compensation reduced the mean absolute lateral error by 0.350 m and the mean absolute yaw angle error by 7.026° . Subsequently, the integration of the H_∞ control further reduced the mean absolute lateral error by 0.017 m and the mean absolute yaw angle error by 1.580° . Finally, the integration of the quadratic stability further reduced the mean absolute lateral error by 0.015 m and the mean absolute yaw angle error by 1.099° . It is worth noting that the improvements in accuracy at the last two stages were significantly smaller than that of the first stage. This was because the feed-forward control included compensation for path curvature disturbance, which was much larger than the other disturbances.

After adding the disturbance observer-based compensation, the combination of LQR control and quadratic stability exhibited higher path-tracking accuracy compared to the combination of LQR and H_∞ control. For example, when $R_{rr} = 1.2$ m, the mean absolute lateral error and the mean absolute yaw angle error under the former were 0.049 m and 2.401° , respectively. These values indicated reductions of 10.9 % and 35.3 %, respectively, compared to the latter. This was because the

control system based on LQR control inherently suppressed high-frequency disturbances, and after integrating the low-frequency disturbance observer-based feed-forward control, the impact of the remaining low-frequency disturbances on tracking accuracy was relatively smaller than that of the perturbation parameters.

Subsequently, to investigate the adaptability of the proposed controller to path curvature, the tracking errors under different desired path radii were compared. As shown in Tables 7 and 8, the tracking errors of the proposed controller were smaller than those of the other controllers for all three desired path radii and maintain relatively low values. Therefore, the proposed controller exhibited strong adaptability to path curvature. Additionally, when $R_r = 1.6$ m, the proposed controller achieved the smallest tracking error compared to the other two desired radii. This was because q_1 and q_2 were fixed in the controller design, and different error weights had varying adaptability to the desired path curvature. Furthermore, it is worth noting that the effects of increased desired path curvature on the path-tracking control performance were approximately equivalent to those of increased speed, as both led to greater dynamic variations that challenged the controller in maintaining accurate tracking. Therefore, the above findings also indirectly reflected the strong adaptability of the proposed controller to the transplanter's speed.

Overall, each component of the controller proposed in this paper improved the accuracy of curved path-tracking control for the rice transplanter based on the LQR control. Among these components, low-frequency observer-based feed-forward control had the most significant impact on accuracy improvement, followed by quadratic stability, and lastly, H_∞ control. Furthermore, the path-tracking controller proposed in this paper demonstrated strong adaptability to different path curvatures, ensuring that the unmanned rice transplanter achieved the required accuracy for curved path-tracking during headland turns.

4. Conclusions

In this paper, a curved path-tracking control method is proposed for

unmanned rice transplanters during headland turns, aiming to enhance row spacing precision during rice transplanting operations. Specifically, a transplanter steering model and a tracking error model based on the transplanting arm array centre were developed. Furthermore, an integrated robust controller was designed by combining disturbance observer-based feedforward control, LQR, H_∞ control, and quadratic stability, where the LQR ensures system convergence rate, and the other components guarantee robustness against disturbances and parameter uncertainties. Experimental validation confirmed that the proposed method improved the accuracy of steering modelling and path tracking of the rice transplanter. In addition, ablation experiments validated the effectiveness of each component of the control scheme. Overall, the proposed method had high tracking accuracy and satisfied the operational requirements of unmanned rice transplanters. Future research will focus on extending the control design to coupled lateral-longitudinal tracking.

CRediT authorship contribution statement

Yueqi Ma: Writing – review & editing, Writing – original draft, Validation, Software, Methodology, Investigation, Formal analysis. **Guohui Fu:** Validation, Investigation. **Chao Ban:** Validation, Investigation. **Tong Su:** Investigation. **Ruijuan Chi:** Supervision, Methodology, Investigation, Funding acquisition.

Declaration of competing interest

The authors declare that they have no known competing financial interests or personal relationships that could have appeared to influence the work reported in this paper.

Acknowledgment

This work was supported by the National Natural Science Foundation of China under Grant 52172396.

Appendices.

Appendix A

Proof: In Eq. (13), substitute $K = FP^{-1}$ into $AP + BF + (AP + BF)^T + I < 0$, a form satisfying the first LMI in Lemma 1 can be derived as follows:

$$(A + BK)P + P(A + BK)^T + I < 0 \quad (20)$$

Employing the Schur complement lemma (Boyd et al., 1994) in $\begin{bmatrix} -Z & DP \\ (DP)^T & -P \end{bmatrix} < 0$, a form satisfying the second LMI in Lemma 1 can be derived as follows:

$$DPD^T - Z < 0 \quad (21)$$

thus completing the proof.

Appendix B

Proof: In Eq. (16), multiply both sides of the first LMI by $\text{diag}(P^{-1}, I, I)$ on the left and right to obtain:

$$\begin{bmatrix} P^{-1}(\tilde{A}P + \tilde{B}F)P^{-1} + P^{-1}(\tilde{A}P + \tilde{B}F)^TP^{-1} & P^{-1}C & P^{-1}(\tilde{D}P)^T \\ C^TP^{-1} & -\gamma_\infty I & 0 \\ \tilde{D}PP^{-1} & 0 & -\gamma_\infty I \end{bmatrix} < 0 \quad (22)$$

Substitute $K = FP^{-1}$ into Eq. (22) to obtain:

$$\begin{bmatrix} P^{-1}(\tilde{A} + \tilde{B}K) + (\tilde{A} + \tilde{B}K)^TP^{-1} & P^{-1}C^T & \tilde{D}^T \\ CP^{-1} & -\gamma_\infty I & 0 \\ \tilde{D} & 0 & -\gamma_\infty I \end{bmatrix} < 0 \quad (23)$$

Eq. (23) satisfies the condition required by Lemma 1, thereby establishing the proof.

Appendix C

Proof: Considering that all elements in K are all negative, and that the absolute values of the control input and that of its rate of change must be smaller than their upper bounds, there is $\begin{cases} -K|X_{\max}| < |U_{\max}| \\ -K|\dot{X}_{\max}| < |\dot{U}_{\max}| \end{cases}$ (24)

Given $K = FP^{-1}$, thus:

$$\begin{cases} FP^{-1}|X_{\max}| > -|U_{\max}| \\ FP^{-1}|\dot{X}_{\max}| > -|\dot{U}_{\max}| \end{cases} \quad (25)$$

Due to the presence of nonlinear terms in Eq. (25), transforming it into LMIs using the Schur complement yields:

$$\begin{cases} \begin{bmatrix} -|U_{\max}| & F \\ |X_{\max}| & P \end{bmatrix} < 0 \\ \begin{bmatrix} -|\dot{U}_{\max}| & F \\ |\dot{X}_{\max}| & P \end{bmatrix} < 0 \end{cases} \quad (26)$$

Thereby establishing the proof.

References

- Bhat, V. S., & Wang, Y. (2025). Revisiting the control systems of autonomous vehicles in the agricultural sector: A systematic literature review. *IEEE Access*, 13, 54686–54721. <https://doi.org/10.1109/access.2025.3555142>
- Boyd, S., Ghaoui, L. E., Feron, E., & Balakrishnan, V. (1994). *Linear matrix inequalities in system and control theory*. Philadelphia, PA, USA: Society for Industrial and Applied Mathematics.
- Dekhterman, S. R., Cichon, M. T., Norris, W. R., Nottage, D., & Soylemezoglu, A. (2024). Hierarchical rule-based reduction fuzzy control for constant velocity path-tracking of a differential steer vehicle. *Journal of Field Robotics*, 41(3), 718–734. <https://doi.org/10.1002/rob.22287>
- Fukumoto, T., Chida, Y., & Tanemura, M. (2022). Improved tracking performance by H_∞ control for an automatic spinach harvester. *IFAC-PapersOnLine*, 55(25), 265–270. <https://doi.org/10.1016/j.ifacol.2022.09.357>
- Gagliardi, G., Casavola, A., & Toscano, S. (2022). Linear parameter varying control strategies for combined longitudinal and lateral dynamics of autonomous vehicles. In *Proceedings of the 2022 european control conference (ECC)* (pp. 181–186). London, United Kingdom: IEEE. <https://doi.org/10.23919/ecc55457.2022.9838177>
- Gang, M., Kim, H. J., Jeon, C. W., & Yun, C. (2022). Design and testing of headland turning algorithms based on transition distance prediction for autonomous rice transplanter. *J. ASABE*, 65(6), 1277–1291. <https://doi.org/10.13031/ja.14952>
- Ge, Z. K., Man, Z. H., Wang, Z., Bai, X., Wang, X., Bai, X. P., Wang, X. X., Feng, X., & Li, D. Q. (2023). Robust adaptive sliding mode control for path-tracking of unmanned agricultural vehicles. *Computers & Electrical Engineering*, 108, Article 108693. <https://doi.org/10.1016/j.compeleceng.2023.108693>
- Gökçe, B., Koca, Y. B., Aslan, Y., & Gökçe, C. O. (2021). Particle swarm optimization-based optimal PID control of an agricultural Mobile robot. *Comptes Rendus de l'Académie Bulgare des Sciences*, 74(4), 568–575. <https://doi.org/10.7546/CRABS.2021.04.12>
- Gong, J. W., Jiang, Y., & Xu, W. (2014). *Model predictive control for self-driving vehicles*. Beijing: Beijing Institute of Technology Press (in Chinese).
- Han, X., Kim, H. J., Jeon, C. W., Moon, H. C., Kim, J. H., & Yi, S. Y. (2019). Application of a 3D tractor-driving simulator for slip estimation-based path-tracking control of auto-guided tillage operation. *Biosystems Engineering*, 178, 70–85. <https://doi.org/10.1016/j.biosystemseng.2018.11.003>
- He, J., Hu, L., Wang, P., Liu, Y., Man, Z., Tu, T., Yang, L. N., Li, Y. Y., Yi, Y. L., Li, W. C., & Luo, X. (2022). Path-tracking control method and performance test based on agricultural machinery pose correction. *Computers and Electronics in Agriculture*, 200, Article 107185. <https://doi.org/10.1016/j.compag.2022.107185>
- Hu, C., Ru, Y., Li, X., Fang, S., Zhou, H., Yan, X., Liu, M., & Xie, R. (2024). Path tracking control for brake-steering tracked vehicles based on an improved pure pursuit algorithm. *Biosystems Engineering*, 242, 1–15. <https://doi.org/10.1016/j.biosystemseng.2024.04.006>
- Ji, X., Ding, S., Wei, X., & Cui, B. (2023). Path-tracking of unmanned agricultural tractors based on a novel adaptive second-order sliding mode control. *Journal of the Franklin Institute*, 360(8), 5811–5831. <https://doi.org/10.1016/j.jfranklin.2023.03.053>
- Lee, K., Jeon, S., Kim, H., & Kim, D. (2019). Optimal path-tracking control of autonomous vehicle: Adaptive full-state linear quadratic gaussian (LQG) control. *IEEE Access*, 7, 109120–109133. <https://doi.org/10.1109/ACCESS.2019.2933895>
- Legrand, R., Claveau, F., Chevrel, P., Rancinangue, B., & Dollet, A. (2022). H_2/H_∞ robust lateral control of an off-road two-steering-axle vehicle on slippery sloping soils. *IFAC - Papers On Line*, 55(25), 187–192. <https://doi.org/10.1016/j.ifacol.2022.09.345>
- Li, Y. M., Wu, T., Xiao, Y. F., Gong, L., & Liu, C. L. (2023). Path planning in continuous adjacent farmlands and robust path-tracking control of a rice-seeding robot in paddy field. *Computers and Electronics in Agriculture*, 210, Article 107900. <https://doi.org/10.1016/j.compag.2023.107900>
- Liu, W. X. (2001). *Automotive Design*. Beijing, China: Tsinghua University Press (in Chinese).
- Manikandan, S., Kaliyaperumal, G., Hakak, S., & Gadekallu, T. R. (2022). Curve-aware model predictive control (C-MPC) trajectory tracking for automated guided vehicle (AGV) over on-road, in-door, and agricultural-land. *Sustainability*, 14(19), 12021. <https://doi.org/10.3390/su141912021>
- Miao, L. D., Zhang, Z., Wu, X. H., Shi, P. L., Xu, J. C., Li, B., Gao, B. H., & Qu, S. (2017). Analysis of automotive tyre forces for non ackermann geometry (in Chinese, with English abstract). *Science Technology and Engineering*, 17(31), 359–363. Retrieved from <http://www.stae.com.cn/jsygc/article/abstract/1703337>
- Oh, K., & Seo, J. (2022). Development of a sliding-mode-control-based path-tracking algorithm with model-free adaptive feedback action for autonomous vehicles. *Sensors*, 23(1), 405. <https://doi.org/10.3390/s23010405>
- Rath, B. N., & Subudhi, B. (2022). A robust model predictive path following controller for an autonomous underwater vehicle. *Ocean Engineering*, 244, Article 110265. <https://doi.org/10.1016/j.oceaneng.2021.110265>
- Shojaei, K., & Taghavifar, H. (2022). Input-output feedback linearisation control of a tractor with n-trailers mechanism considering the path curvature. *Proceedings - Institution of Mechanical Engineers, Part C (Mechanical Engineering Science)*, 236(17), 9700–9715. <https://doi.org/10.1177/0954406221088236>
- Song, Y., Xue, J., Zhang, T., Sun, X., Sun, H., Gao, W., & Chen, Q. (2025). Path tracking control of crawler tractor based on adaptive adjustment of lookahead distance using sparrow search algorithm. *Computers and Electronics in Agriculture*, 234, Article 110219. <https://doi.org/10.1016/j.compag.2025.110219>
- Trendafilov, K., & Tihanov, G. (2022). Comparative analysis of the headland width when making T-turns by a mounted machine-tractor unit on an irregularly-shaped field. *INMATEH - Agricultural Engineering*, 67(2), 221–232. <https://doi.org/10.35633/inmateh-67-22>
- Wu, S., Wan, J., Chen, Z., Liao, L., Xiao, K., & Wang, P. (2022). LQG/LTR controller design for power control of small pressurized water reactors under four feedback-controlled strategies. *Nuclear Science and Engineering*, 197(4), 660–675. <https://doi.org/10.1080/00295639.2022.2122304>
- Xu, G., Chen, M., He, X., Pang, H., Miao, H., Cui, P., Wang, W. J., & Diao, P. (2021). Path following control of tractor with an electro-hydraulic coupling steering system: Layered multi-loop robust control architecture. *Biosystems Engineering*, 209, 282–299. <https://doi.org/10.1016/j.biosystemseng.2021.07.014>
- Yang, Y., Li, Y., Wen, X., Zhang, G., Ma, Q., Cheng, S., Qi, J., Xu, L. Y., & Chen, L. (2022). An optimal goal point determination algorithm for automatic navigation of agricultural machinery: Improving the tracking accuracy of the pure pursuit algorithm. *Computers and Electronics in Agriculture*, 194, Article 106760. <https://doi.org/10.1016/j.compag.2022.106760>
- Yang, L., Yue, M., & Ma, T. (2019). Path following predictive control for autonomous vehicles subject to uncertain tyre-ground adhesion and varied road curvature. *International journal of control. Automation Syst.*, 17(1), 193–202. <https://doi.org/10.1007/s12555-017-0457-8>
- Zhou, K., Doyle, J. C., & Glover, K. (1996). *Robust and optimal control*. Upper Saddle River, NJ, USA: Prentice Hall.
- Zhou, B., Su, X., Yu, H., Guo, W., & Zhang, Q. (2023). Research on path tracking of articulated steering tractor based on modified model predictive control. *Agriculture*, 13(4), 871. <https://doi.org/10.3390/agriculture13040871>
- Zhou, J., Wen, J., Yao, L., Yang, Z., Xu, L., & Yao, L. (2025). Agricultural machinery path tracking with varying curvatures based on an improved pure-pursuit method. *Agriculture*, 15(3), 266. <https://doi.org/10.3390/agriculture15030266>